DOI: 10.1002/ ((please add manuscript number))
Article type: Full Paper

High thermoelectric performance in *p*-type polycrystalline Cd-doped SnSe achieved by a combination of cation vacancies and localized lattice engineering

Xiaolei Shi, Angyin Wu, Tianli Feng, Kun Zheng, Weidi Liu, Qiang Sun, Min Hong, Sokrates T. Pantelides, Zhi-Gang Chen, and Jin Zou**

X-L. Shi, A-Y. Wu, W-D. Liu, Q. Sun, Prof. Z-G. Chen and Prof. J. Zou
Materials Engineering, the University of Queensland, Brisbane, QLD 4072, Australia
E-mail: zhigang.chen@uq.edu.au; j.zou@uq.edu.au
T. Feng, Prof. S. T. Pantelides
Department of Physics and Astronomy and Department of Electrical Engineering and Computer Science, Vanderbilt University, Nashville, Tennessee 37235, USA
Materials Science and Technology Division, Oak Ridge National Laboratory, Oak Ridge, Tennessee 37831, USA
Prof. K. Zheng
Beijing Key Lab of Microstructure and Property of Solids, Institute of Microstructure and Properties of Advanced Materials, Beijing University of Technology, Beijing 100124, China
M. Hong, Prof. Z-G Chen
Centre for Future Materials, University of Southern Queensland, Springfield central, QLD 4300, Australia
E-mail: zhigang.chen@usq.edu.au;
Prof. J. Zou
Centre for Microscopy and Microanalysis, the University of Queensland, Brisbane, QLD 4072, Australia

Keywords: thermoelectric, solvothermal, tin selenide, Cd-doping, characterization.

Abstract:

In this work, we report a high figure of merit (*ZT*) of ~1.7 at 823 K in *p*-type polycrystalline Cd-doped SnSe by combining cation vacancies and localized-lattice engineering. It is observed that the introduction of Cd atoms in SnSe lattice induce Sn vacancies, which act as *p*-

type dopants. A combination of facile solvothermal synthesis and fast spark plasma sintering technique boosts the Sn vacancy to a high level of ~2.9 %, which results in an optimum hole concentration of ~2.6×10^{19} cm^{-3} and an improved power factor of ~6.9 μW cm^{-1} K^{-2}. Simultaneously, a low thermal conductivity of ~0.33 W m^{-1} K^{-1} is achieved by effective phonon scattering at localized crystal imperfections, as observed by detailed structural characterizations. Density-functional-theory calculations reveal that the role of Cd atoms in the SnSe lattice is to reduce the formation energy of Sn vacancies, which in turn lower the Fermi level down into the valence bands, generating holes. This work explores the fundamental Cd-doping mechanisms at the nanoscale in a SnSe matrix and demonstrates vacancy and localized-lattice engineering as an effective approach to boosting thermoelectric performance. The work provides an avenue in achieving high-performance thermoelectric properties of materials.

1. Introduction

By converting heat into electricity, thermoelectric materials provide a potential solution to the world energy crisis as well as to environmental issues that arise from fossil fuels.[1-4] The energy conversion efficiency of thermoelectric materials is measured by the dimensionless figure of merit $ZT = S^2\sigma T/\kappa = S^2\sigma T/(\kappa_e + \kappa_l)$,[3] where σ, S, $S^2\sigma$, T, κ, κ_e, and κ_l are the electric conductivity, the Seebeck coefficient, the power factor, the absolute temperature, the total thermal conductivity, and the electronic and lattice thermal conductivities,[5, 6] respectively. To date, two major strategies for achieving high ZT are optimizing the power factor and reducing κ_l by band and structural engineering, respectively.[7, 8]

Stannous selenide (SnSe) has attracted much attention because of its great potential in realizing high-performance, low-toxic and low-cost thermoelectric devices.[3, 9-13] Spectacularly high peak *ZTs* of ~2.6 at 923 K[14] and ~2.8 at 773 K[15] were reported in *p*-type and *n*-type SnSe single crystals, owing to their high power factor and remarkably low thermal conductivity along specified crystal directions.[14, 15] However, due to the special demands of crystal-growth techniques, prospective high cost for production, and undesirable mechanical properties,[10, 16] SnSe single crystals are not well-suited for thermoelectric devices and have considerable limitations for industrial scale-up.[15, 17, 18] Besides, there are critical controversies on the reported high *ZT*s in single-crystal SnSe[19, 20] because the mass densities of experimental samples are much smaller than the theoretical density of SnSe.[20] In this context, polycrystalline SnSe has become a promising alternative candidate.[3, 7, 21, 22] To improve the relatively low power factor and reduce the high thermal conductivity of polycrystalline SnSe,[17] three major strategies including doping,[3, 7, 23] multi-phase alloying[3, 24] and micro/nanoscale texturing[3, 25] have been employed. The peak *ZT*s have been improved from ~0.5 to ~1.5 before 850 K.[3] Considering that SnSe is easy to volatilize Se and become unstable at higher temperature, it has

been a challenge to improve *ZT* even higher to *ZT* >1.5 before 850 K, which is necessary for device applications.[18, 26, 27]

In order to achieve high-*ZT* polycrystalline SnSe, a key step is to tune an appropriate carrier concentration *n*, which optimizes the electrical transport properties.[3, 28] In solution-based synthesis routes such as hydrothermal[3] and solvothermal[3, 29] syntheses, the cation and/or anion vacancy concentrations can be controlled by tuning the synthesis parameters such as the stoichiometric ratio of precursors, synthesis temperature, synthesis pressure, and potential of hydrogen (pH) level according to the reaction kinetics and/or thermodynamics.[3, 30] "Vacancy engineering" is an effective strategy to tune *n* and ultimately enhance *ZT*s of polycrystalline SnSe because Sn vacancies are known to dope SnSe *p*-type, and Se vacancies are known to dope SnSe *n*-type.[3] For *p*-type SnSe, however, to achieve an optimal Sn vacancy level has historically been difficult.[31-34] A previous study found that heavy Na^+ doping achieved a high maximum Sn vacancy level of ~2 %, which induces a hole carrier concentration $p = \sim 1.5\times10^{19}$ cm^{-3} and a relatively high *ZT* = ~1.36 at 823 K.[7] However, such *ZT* is still not optimal since 2 % Sn vacancies are not sufficient for the desired *p*,[7] while higher Na^+ concentration could not further increase the Sn vacancy concentration because Na^+ does not act as dopant but only triggers Sn-vacancy formation.[7] Therefore, it is necessary to seek an appropriate dopant that has stable +2 valence state (same to Sn^{2+}) as well as a different atomic/ionic size because the size difference can result in lattice heterogeneity (dilatation or contraction),[21, 23] which can weaken the bonding ability of Sn and Se and expand the maximum cation vacancy level. Meanwhile, such lattice heterogeneity can also reduce κ_l by increasing the phonon scattering with nanoscale crystal imperfections such as point defects and lattice distortions.[31-34]

In this study, we choose Cd as dopant to meet the requirements listed above since Cd is an ideal candidate with stable 2+ valence state and different atomic/ionic size (0.166/0.095 nm) compared to Sn/Sn^{2+} (0.151/0.112 nm).[35] We design a facile solvothermal synthesis route with a fast spark plasma sintering (SPS) technique to fabricate polycrystalline Cd-doped SnSe, as shown in **Figure 1 (a, b)**, respectively. Comprehensive compositional investigations including X-ray photoelectron spectroscopy (XPS), electron probe micro-analyzer (EPMA), and energy dispersive spectroscopy (EDS) demonstrated that our Cd doping achieved a high cation vacancy concentration of ~2.9 %, leading to an increased $p = \sim 2.6\times10^{19}$ cm^{-3}, and in turn an improved $S^2\sigma$ of ~6.9 μW cm^{-1} K^{-2} at 823 K. Besides, extensive structural and morphological characterizations including XPS, X-ray diffraction (XRD), scanning electron microscopy (SEM), transmission electron microscopy (TEM) with spherical aberration-corrected scanning TEM (Cs-corrected STEM) indicate that the Cd doping can result in localized crystal imperfections including localized lattice distortions and strains, dislocations, and nanoscale vacancy domains (illustrated in **Figure 1(c)**). These defects lead to a low κ_l of ~0.33 W m^{-1} K^{-1} and in turn a high peak *ZT* of ~1.7 at 823 K, which is a record value at this temperature compared with reported studies, as shown in **Figure 1(d)**. Furthermore, a competitive *ZT* of ~1.3 at 773 K before the phase transition temperature (800 K) and a high average *ZT* of 0.84 for the entire temperature range can be simultaneously achieved, showing that the polycrystalline Cd-doped SnSe has considerable potential for device applications. In fact, this study serves as an exploration of the fundamental Cd-doping mechanisms at the nanoscale in a SnSe matrix, and describes a novel concept to realize high *ZT* in polycrystalline SnSe.

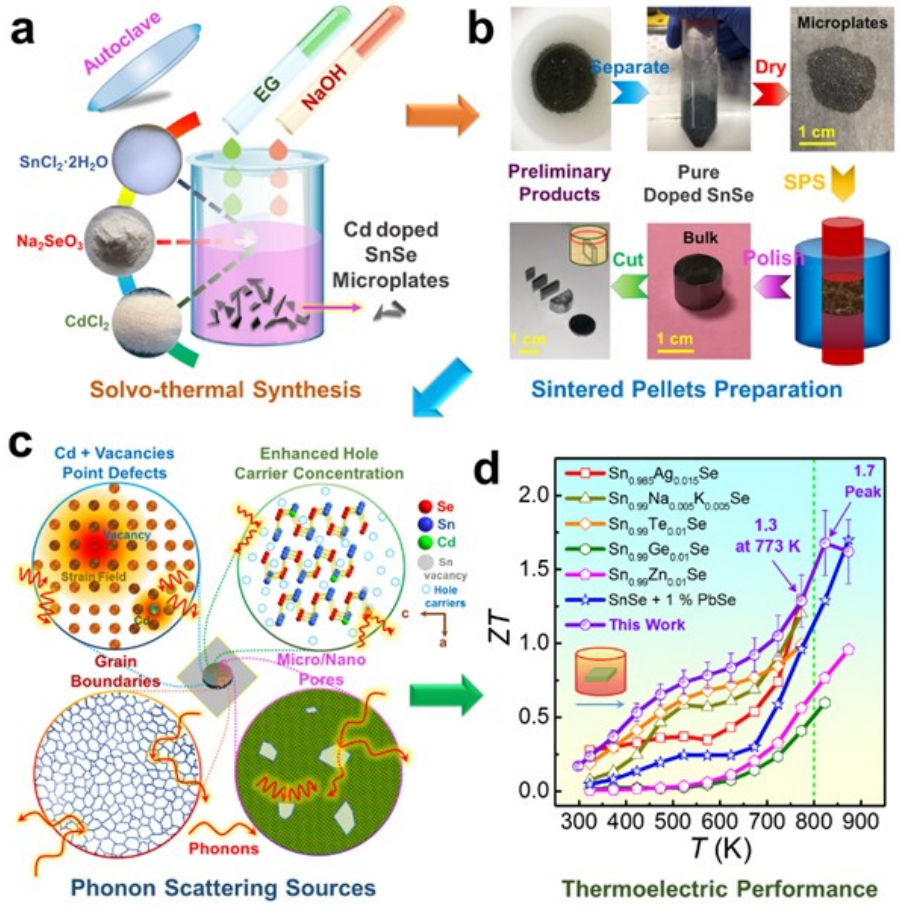

Figure 1. Illustrations of fabrication for our Cd-doped SnSe. (a) Illustration of solvothermal synthesis; (b) obtained Cd-doped SnSe products and subsequent sintering and cutting processes; (c) phonon scattering sources observed in our pellets; and (d) comparisons of achieved temperature-dependent *ZT* from our pellets with reported polycrystalline SnSe.[7, 36-41]

2. Results and Discussion

A suitably large p and low κ are vital for achieving high ZT for polycrystalline SnSe. To predict an suitable p for high ZT, we use a single parabolic band (SPB) model[42-45] to study p-dependent ZT at T = 823 K with a fixed κ_l of 0.4 W m^{-1} K^{-1}, as shown in **Figure 2(a)** (details can be seen in **Section 1** in Supporting Information). It is seen that p = ~3.0×10^{19} cm^{-3} can contribute to a peak ZT of ~1.4, which is competitive to the currently reported polycrystalline SnSe.[3] In terms of thermal conductivity κ, since lattice vibrations (κ_l) contribute more than 50 % to the total κ in polycrystalline SnSe under 850 K,[7, 14, 21] minimizing κ_l plays a significant role in lowering κ. We have studied p-dependent ZT at T = 823 K with different κ_l values. As shown in **Figure 2(b)**, a high peak ZT of ~1.85 at 823 K can be obtained when κ_l is reduced to 0.2 W m^{-1} K^{-1}, which is close to its minimum value of 0.26 W m^{-1} K^{-1} [46] calculated under the condition of full density along the a-axis.[3] Thus, it is possible to improve ZTs by appropriately tuning p and reducing κ_l.

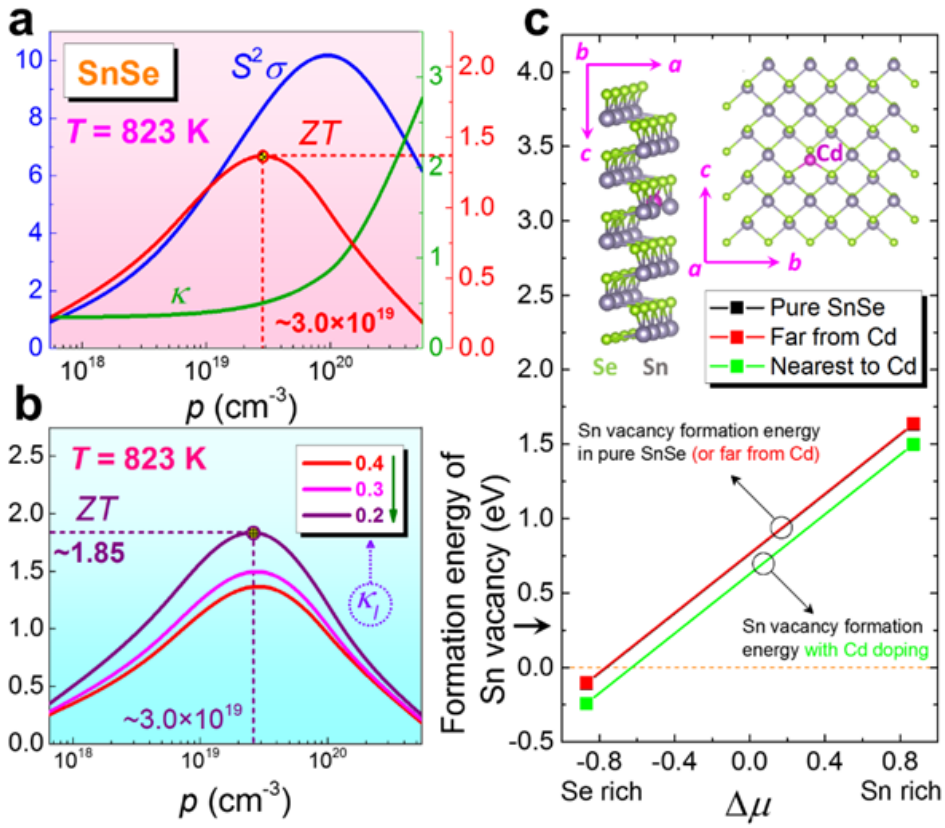

Figure 2. Calculated thermoelectric performance as a function of hole concentration and Sn vacancy formation energy of SnSe. (a) Calculated *p*-dependent *ZT* of polycrystalline SnSe at $T = 823$ K with a fixed κ_l of 0.4; (b) Improvement of *p*-dependent *ZT via* reducing κ_l; (c) Calculated results of Sn vacancy formation energy before and after inducing Cd. The units of $S^2\sigma$ and κ (κ_l) are μW cm^{-1} K^{-2} and W m^{-1} K^{-1}, respectively.

To verify that Cd is an ideal candidate for improving the cation vacancy level, we first explore the solubility of Cd in SnSe, and then study the real compositions of Cd-doped SnSe with different doping concentrations, as shown in **Table 1**. In this study, we use $SnCl_2{\cdot}2H_2O$, Na_2SeO_3 and $CdCl_2$ as precursors to fabricate Cd-doped SnSe. We first define the mole percentage (x) of $CdCl_2$ in $SnCl_2{\cdot}2H_2O$. The nominal compositions of Cd-doped SnSe can then be described as $Sn_{1-x}Cd_xSe$,

where the selected x values are 0 % (no $CdCl_2$ added), 0.5 %, 1 %, 1.5 %, 2 %, 2.5 %, 3 %, and 3.5 % as listed in **Table 1**. Through detailed EDS and EPMA studies, however, it was found that the real compositions of the synthesized products are different from the nominal compositions, as shown in **Table 1**. With increasing x, the cation vacancy level gradually increases until reaching a maximum value of 2.9 %, from which a solubility limit of Cd (~2.3 %) is achieved when the real composition is $Sn_{0.948}Cd_{0.023}Se$. The instrumental error of EMPA is ~0.1 %, which demonstrates a high accuracy. These results indicate that Cd doping has great potential for further increasing the cation vacancy level and hence the hole concentration as well as enhancing *ZT*.

Table 1. Comparisons of measured real compositions *via* EPMA with nominal composition ($Sn_{1-x}Cd_xSe$). The corresponding vacancy rates (%) are also included.

Nominal Composition ($Sn_{1-x}Cd_xSe$)	Real Composition via EPMA	Vacancy (%)
SnSe	$Sn_{0.994}Se$	0.6
$Sn_{0.995}Cd_{0.005}Se$	$Sn_{0.984}Cd_{0.005}Se$	1.1
$Sn_{0.99}Cd_{0.01}Se$	$Sn_{0.976}Cd_{0.009}Se$	1.5
$Sn_{0.985}Cd_{0.015}Se$	$Sn_{0.966}Cd_{0.014}Se$	2.0
$Sn_{0.98}Cd_{0.02}Se$	$Sn_{0.957}Cd_{0.019}Se$	2.4
$Sn_{0.975}Cd_{0.025}Se$	$Sn_{0.948}Cd_{0.023}Se$	2.9
$Sn_{0.97}Cd_{0.03}Se$	$Sn_{0.948}Cd_{0.023}Se$	2.9
$Sn_{0.965}Cd_{0.035}Se$	$Sn_{0.948}Cd_{0.023}Se$	2.9

To understand the impact of Cd atoms on Sn-vacancy formation, we performed density functional theory (DFT) calculations using SnSe supercells (256 atoms) with and without a Cd atom occupying the Sn site. The results are shown in **Figure 2(c)**. We find that the Sn vacancy formation energy in pure SnSe lattice is about 1.63 eV (with respect to the chemical potential of Sn metal). After a Cd atom is introduced in the lattice by occupying a cation site, we re-calculate the Sn vacancy formation

energies. We find that for the Sn atoms that are far from the Cd atom, the vacancy formation energy remains the same as expected. For the Sn atom that is nearest to the Cd atom, the vacancy formation energy is 1.50 eV, reducing by 0.13 eV, which is much larger than the room-temperature thermalization energy 0.026 eV. Therefore, the DFT results explicitly support the experimental observation that Cd dopants can facilitate the formation of Sn vacancies in SnSe. It should be mentioned that secondary phase (mainly CdSe) was identified after the doping level reached the Cd solubility in SnSe. However, the ultrasonic separation technique can effectively remove the secondary phase after the synthesis, as confirmed in **Figure S2**.[7, 21, 23]

Table 1 indicates that Cd-doping can further improve the hole concentration *p*, but it is still unclear if such improvement is caused by the Cd atoms themselves or the induced Sn vacancies. To gain insight into the mechanism of the increase of the hole concentration, we have performed DFT calculations on the electronic band structure evolution for SnSe after Cd-doping with and without cation vacancy. **Figure 3(a-d)** compares the calculated band structures of pure SnSe (with the supercell of $Sn_{128}Se_{128}$), Cd-doped SnSe without vacancies ($CdSn_{127}Se_{128}$), Cd-doped SnSe with one Sn vacancy ($CdSn_{126}Se_{128}$), and SnSe with one Sn vacancy without Cd, respectively. **Figure 3(e)** compares their corresponding density of states (DOSs). We find that the band structures and DOSs are almost identical with and without Cd replacing Sn, with the only difference being that the degenerate bands in the perfect SnSe lattice split after a Cd atom is introduced. This difference originates from the breaking of the supercell symmetry by the Cd impurity and has negligible impact on the hole concentration.[3] In contrast, for the pure SnSe and Cd-doped SnSe with an extra Sn vacancy introduced, the Fermi level moves into the valence band, making the material a degenerate semiconductor with significantly increased hole concentration. Therefore, we conclude that it is the Sn vacancies rather than the Cd atoms that introduce holes in SnSe. The role of Cd atoms is to increase the Sn vacancy concentration. More discussion about the effect of Cd-doping on conduc-

tion band of SnSe is shown in **Figure S1** in Supporting Information.

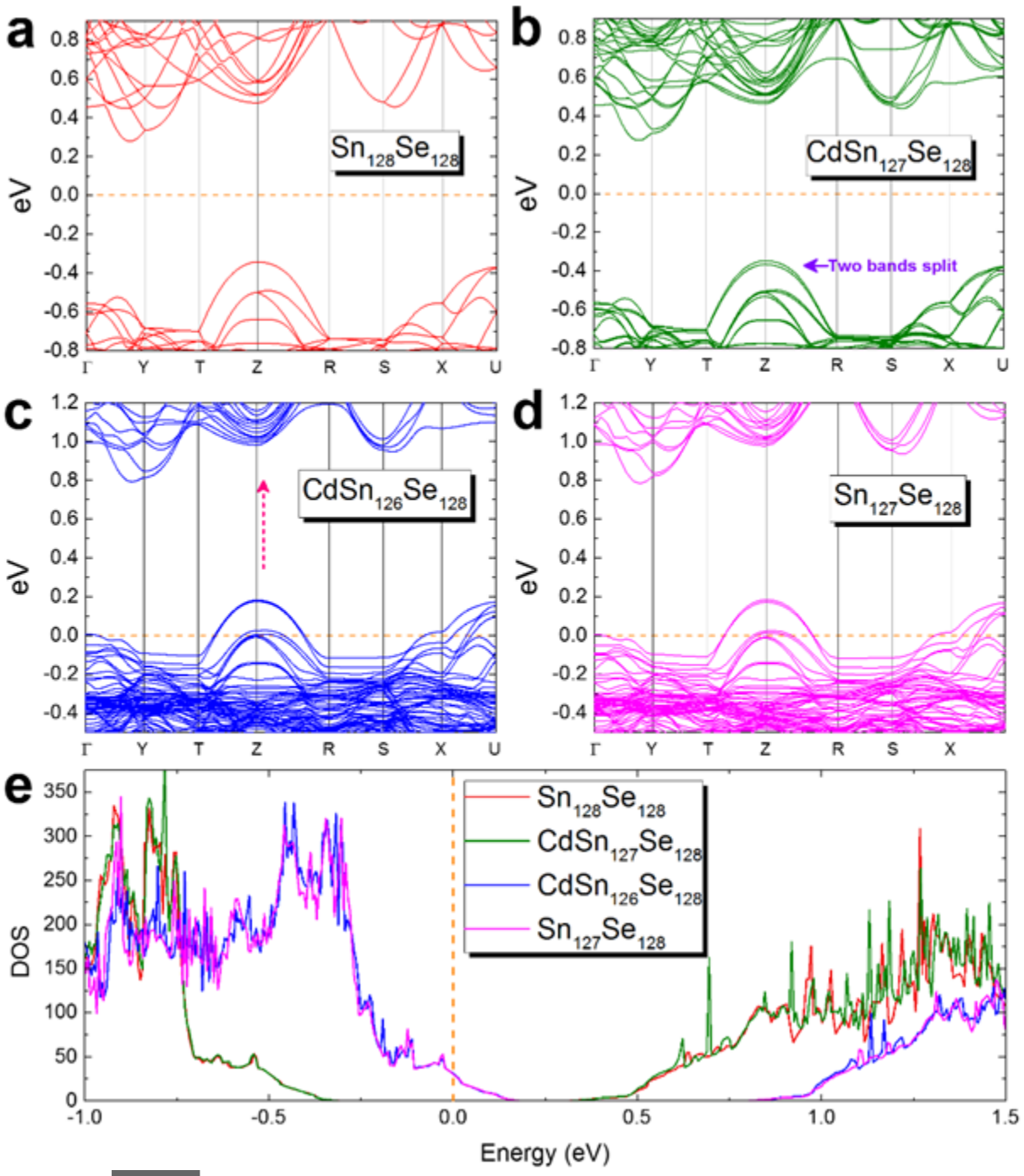

Figure 3. Band structures and DOS of SnSe. Comparisons of calculated electronic structures of (a) pure SnSe ($Sn_{128}Se_{128}$); (b) Cd-doped SnSe without vacancy ($CdSn_{127}Se_{128}$); (c) Cd-doped SnSe with

vacancy ($CdSn_{126}Se_{128}$); (d) SnSe with vacancy ($Sn_{127}Se_{128}$); and (e) Comparisons of corresponding DOS.

Figure 4(a) shows XRD results for our synthesized Cd-doped SnSe with different Cd doping levels. It is clearly seen that all diffraction peaks can be indexed as orthorhombic-structured SnSe and a space group of *Pnma*, according to the JCPDS 48-1224 Standard Identification Card. The strongest diffraction peaks of 400* suggest our products contain significant (100) surfaces.[3, 7, 21, 23] With increasing the Cd doping level, the other diffraction peaks such as 111* become weaker (refer to **Figure S2(b)**), indicating a strengthened anisotropy in the synthesized products.[3, 7, 21] **Figure 4(b)** is magnified 400* diffraction peaks, and shows all peaks shifted toward higher 2θ angles, from $2\theta = 31.081°$ as the standard value, indicating a reduced lattice parameter a,[7, 23, 47] and in turn a shrunken unit cell derived from the Sn vacancies in SnSe.[7] **Figure 4(c, d)** show the calculated lattice parameters a, b, c, and unit cell volume V as functions of the cation vacancy level given in **Table 1**. With increasing vacancy concentration, a, b and c slightly decrease, resulting in a V shrinkage.[48]

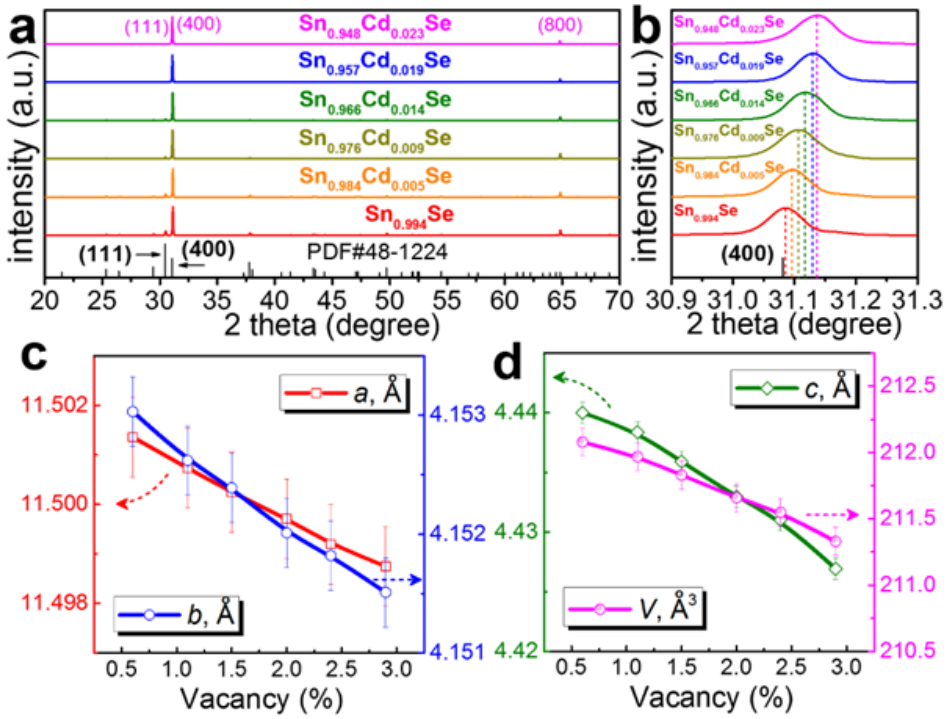

Figure 4. Structural characterizations of synthesized products. (a) XRD results; (b) Enlarged 400* peaks to see the peak deviation. Achieved lattice parameters of (c) *a*, *b*; (d) *c* and *V* as a function of vacancy rate shown in **Table 1**.

Figure 5(a) shows a typical SEM image of the synthesized $Sn_{0.948}Cd_{0.023}Se$ microplates. The inset optical image shows that these microplates have silver-like metallic luster.[7] Compared with their un-doped counterparts shown in **Figure S3**, the most significant surfaces of Cd-doped microplates are also (100). But their average size (124.5 μm measured *via* Nano Measurer software with a sample capacity larger than 1000) is larger than their un-doped counterparts (110.7 μm), indicating a strengthened anisotropy in these Cd-doped microplates,[3, 7] which agrees with the XRD results shown in **Figure 4(a)**. **Figure 5(a)** also shows that the Cd-doped microplates tend to agglomerate to form a flower-like morphology.[21, 25] **Figure 5(b)** shows a typical $Sn_{0.948}Cd_{0.023}Se$ microplate with a (100) surface,

from which pores and slight crystal bent can be seen.[21] A typical pore is shown in the inset of **Figure 5(b)** in a magnified SEM image. **Figure 5(c)** shows one typical $Sn_{0.948}Cd_{0.023}Se$ microplate with lateral surfaces at a microscale as well as the corresponding atomic structure related to the surface features.

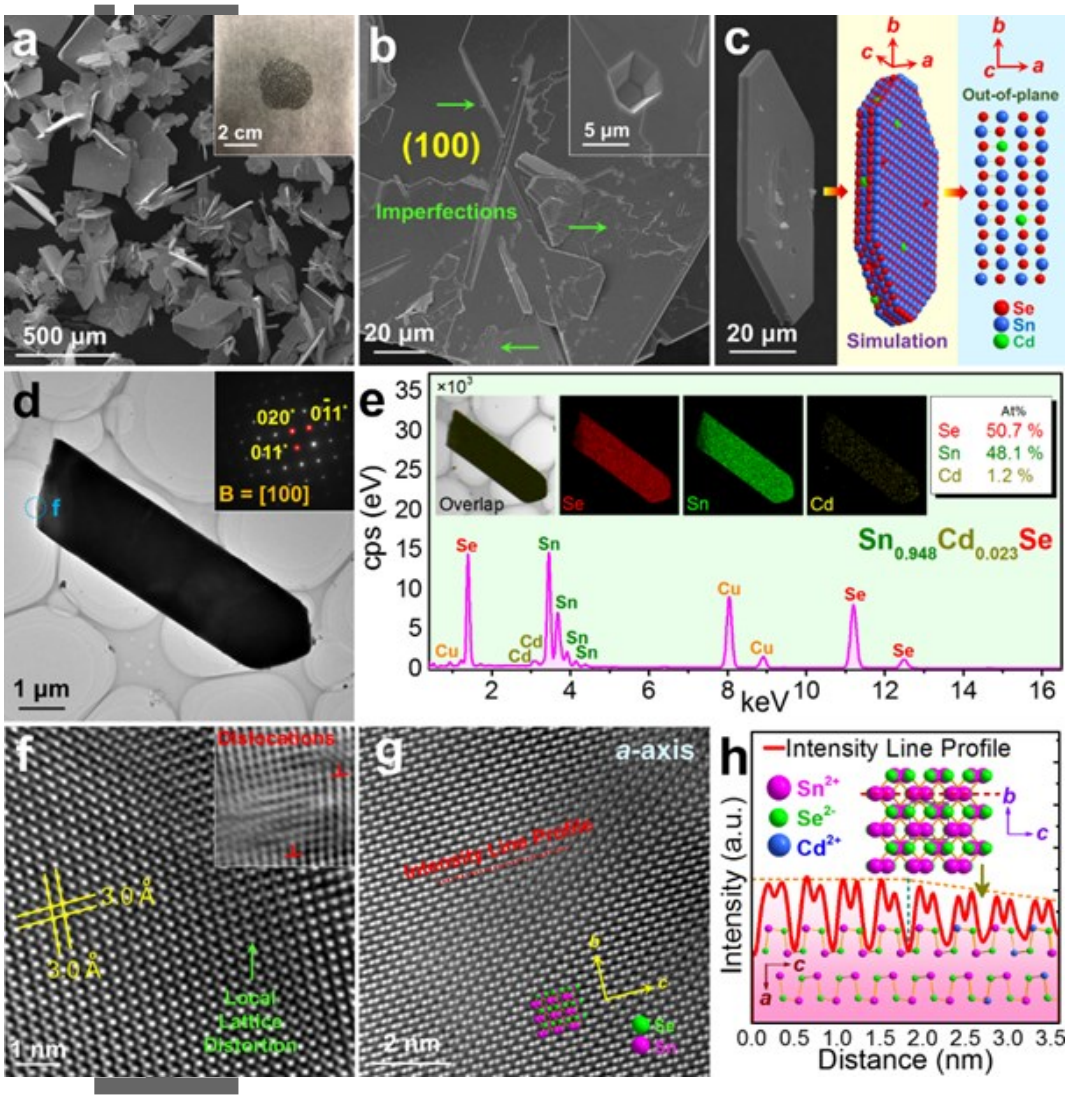

Figure 5. Morphological and compositional characterizations of the synthesized products. (a) SEM image with inset of optical image of synthesized flower-like $Sn_{0.948}Cd_{0.023}Se$ microplates; (b) Magnified SEM image of one $Sn_{0.948}Cd_{0.023}Se$ microplate showing (100) surface with crystal imperfections exemplified in inset; (c) One typical $Sn_{0.948}Cd_{0.023}Se$ microplate with simulated atomic model

showing the out of plane; (d) TEM image of a typical $Sn_{0.948}Cd_{0.023}Se$ microplate with inset of corresponding SAED pattern; (e) EDS spot and mapping images. Cu comes from the TEM copper grid; (f) HRTEM image circled in (d) to see the localized lattice distortion with inset of HRTEM image to see the dislocations; (g) High resolution Cs-STEM HAADF images to see the difference of contrast; (h) Corresponding intensity line profile taken from (g) to illustrate the potential reasons causing the contrast difference.

To further investigate the structural characteristics of the $Sn_{0.948}Cd_{0.023}Se$ microplates, detailed TEM characterization was performed. **Figure 5(d)** shows a [100] zone-axis TEM image for a typical $Sn_{0.948}Cd_{0.023}Se$ plate with the surface perpendicular to the electron beam. The inset corresponding to a selected area electron diffraction (SAED) pattern indicates that the plate has typical orthorhombic structure with a (100) surface,[7, 21] same as the undoped SnSe shown in **Figure S4**. **Figure 5(e)** shows EDS results of **Figure 5(d)**, in which Cd has a uniform distribution at a microscale. **Figure 5(f)** is a high-resolution TEM (HRTEM) image circled in **Figure 5(d)**, showing local lattice distortions and dislocations (inset), which should be derived from the doped Cd with different atomic/ionic size of Sn.[21, 23] **Figure 5(g)** is a STEM high-angle annular dark field (HAADF) image taken along the *a*-axis. The overlays in a normal area show Se atoms in green and Sn atoms in purple and axes. The non-uniform structural contrast suggests a lattice distortion, likely derived from the local elemental variation.[21, 23] **Figure 5(h)** is the intensity line profile (taken along the dashed red line in **Figure 5(g)**, and shows different peak intensities between different areas, reflecting the local compositional variations (such as Cd replacement and cation vacancies).

We sintered the synthesized microplates into pellets to evaluate their thermoelectric performance along different directions, as illustrated in **Figure 1(b)**. Before the evaluation, we performed detailed structural and morphological characterizations on these pellets to confirm the structural and composi-

tional features kept stable after sintering. **Figure 6(a)** shows their XRD patterns (pure SnSe and $Sn_{0.948}Cd_{0.023}Se$) taken along both the ⊥ and // directions. Here "⊥" and "//" mean the directions perpendicular and parallel to the pressure of sintering, respectively. All diffraction peaks can be indexed as orthorhombic-structured SnSe, showing that the structural features remain with no extra phase observed.[21, 23] **Figure 6(b)** magnifies the 111* and 400* peaks to reveal the peak-shifts. It shows the strongest 111* peaks for the sample taken along the // direction and the strongest 400* peaks along the ⊥ direction, demonstrating significant anisotropy in the pellets. Meanwhile, pure SnSe has a slightly stronger 111* peak than $Sn_{0.948}Cd_{0.023}Se$ along the ⊥ direction, indicating more significant anisotropy in $Sn_{0.948}Cd_{0.023}Se$ pellets.[23] Besides, the diffraction peaks taken from the $Sn_{0.948}Cd_{0.023}Se$ pellet move towards a higher 2θ than the peak from pure SnSe, similar to the XRD results shown in **Figure 4(a, b)**. **Figure 6(c)** shows XPS spectra of the $Sn_{0.948}Cd_{0.023}Se$ pellet with a full survey scan, demonstrating the existence of energy states for Se 3*d*, Sn 3*d*, and Cd 3*d*, indicating the successful doping of Cd. Except C and O, no other elements were identified. **Figure 6(d)** shows XPS spectra with a high-resolution scan for Cd $3d_{5/2}$ and Cd $3d_{3/2}$ (peaks at 405 and 412 eV, respectively), showing that only Cd^{2+} valence state exists in the system. These results indicate that the Cd atoms substituted Sn on Sn sites *via* doping, and there is no interstitial atom of Cd in the matrix of SnSe. The quantified at. % of Cd fitted well with the proposed ~2.3 % of Cd.

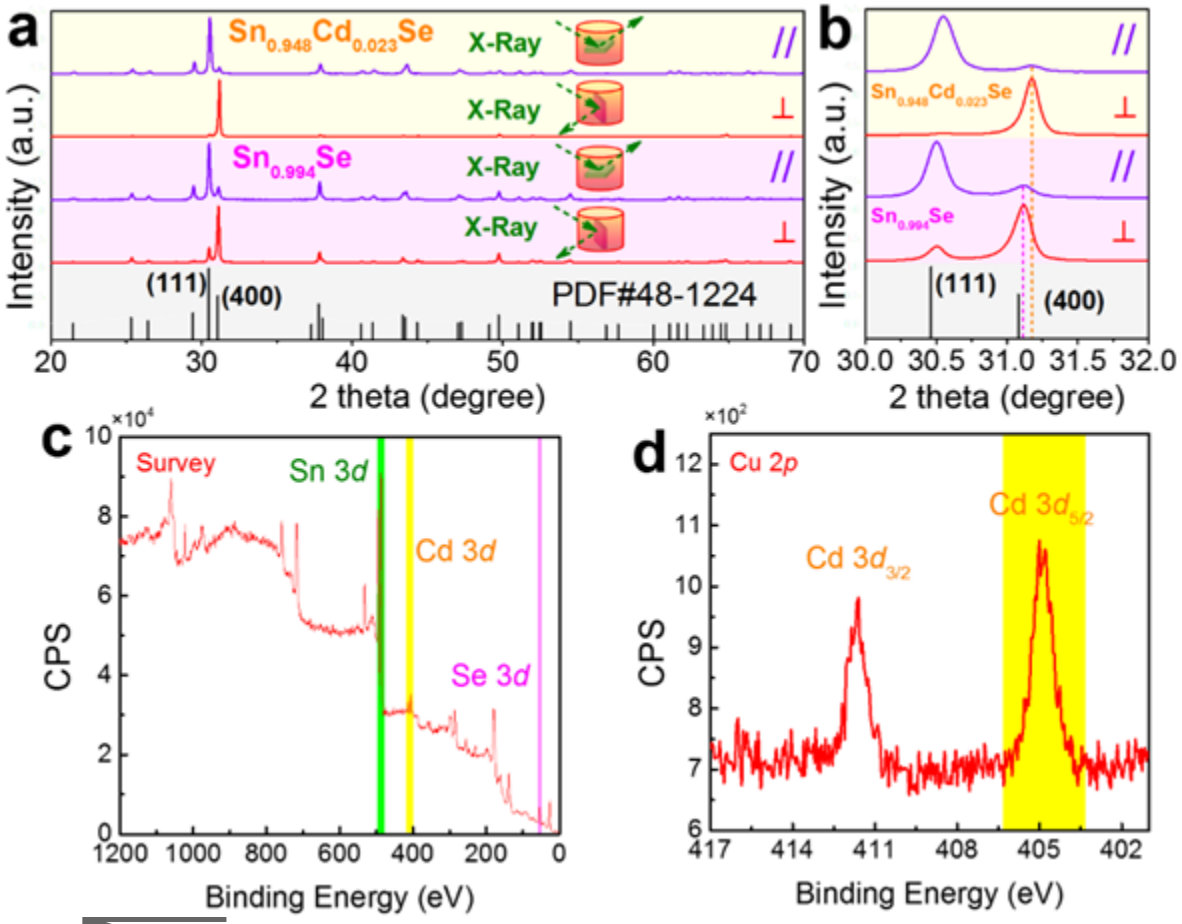

Figure 6. Structural and compositional characterizations of sintered pellets. (a) XRD results of sintered $Sn_{0.994}Se$ and $Sn_{0.948}Cd_{0.023}Se$ pellets measured along different directions; (b) Magnified XRD results to see the deviations of 400* and 111* peak. XPS spectrum of (c) Survey scan for $Sn_{0.948}Cd_{0.023}Se$ pellet and (d) High-resolution scan for Cd 3*d*.

Figure 7(a) is a typical SEM image of a polished surface from a $Sn_{0.948}Cd_{0.023}Se$ pellet (as inset optical image shows), in which a flat surface without any observable flaws can be seen, indicating high compaction in the sintered pellets. **Figure 7(b)** shows corresponding EDS maps, indicating compositional stability after sintering. EPMA studies on the $Sn_{0.948}Cd_{0.023}Se$ pellet indicate that the Sn:Cd:Se ratio is 48.1:1.2:50.7, suggesting a stable composition of $Sn_{0.948}Cd_{0.023}Se$. **Figure 7(c, d)** are SEM im-

ages of pellets, fractured from different directions. Similar to the undoped SnSe (refer to **Figure S5**), the distinct fracture features indicate an obvious anisotropy in the sintered pellets,[7, 21] fitting well with the XRD results shown in **Figure 6(a, b)**. However, different from undoped SnSe pellets, faveolate structures can be occasionally found on the fractured grains of $Sn_{0.948}Cd_{0.023}Se$ pellets, as shown in magnified SEM images in the insets of **Figure 7(c, d)**. These specific structures might be derived from the crystal imperfections of SnSe microplates caused by Cd-doping.[21] **Figure 7(e)** shows a TEM image of our sliced $Sn_{0.948}Cd_{0.023}Se$ pellet, from which obvious overlap of grains can be observed. The inset HRTEM image shows a typical dislocation, indicating that the dislocation still existed after SPS. **Figure 7(f)** shows a [201] zone-axis HRTEM image, in which local lattice distortion is seen. Such local structural variations have been predicted to enhance the phonon scattering and in turn reduce κ_l.[3, 21, 23] **Figure 7(g)** shows STEM HAADF images taken from pure SnSe (left) and $Sn_{0.948}Cd_{0.023}Se$ (right) pellets, respectively, both viewed along their *b*-axes. As can be seen, $Sn_{0.948}Cd_{0.023}Se$ pellets contains nanoscale dark domains, similar to the reported "vacancy domains" caused by Sn vacancies.[32, 49, 50] **Figure 7(h)** is an enlarged STEM HAADF image taken from a typical boundary between normal and dark areas, in which the overlays in a normal area show axes and Se atoms in green and Sn atoms in purple. It is clear that a non-uniform contrast can be seen, suggesting local elemental variation. Besides, no interstitial atom can be found, indicating that there is no interstitial atom of Cd in the matrix of SnSe, supporting to the XPS results. **Figure 7(i)** is the intensity line profile (dashed purple line in **Figure 7(h)** across both normal area and contrast area) taken along the *c*-axis, from which the peak intensities for Se sites keep stable for the entire range, but different peak intensities for Sn sites between normal and dark areas, indicating local elemental variation such as Cd replacing Sn and/or cation vacancies, which can effectively scatter the high-frequency phonons and in turn contribute to a low κ_l.[3, 21, 23]

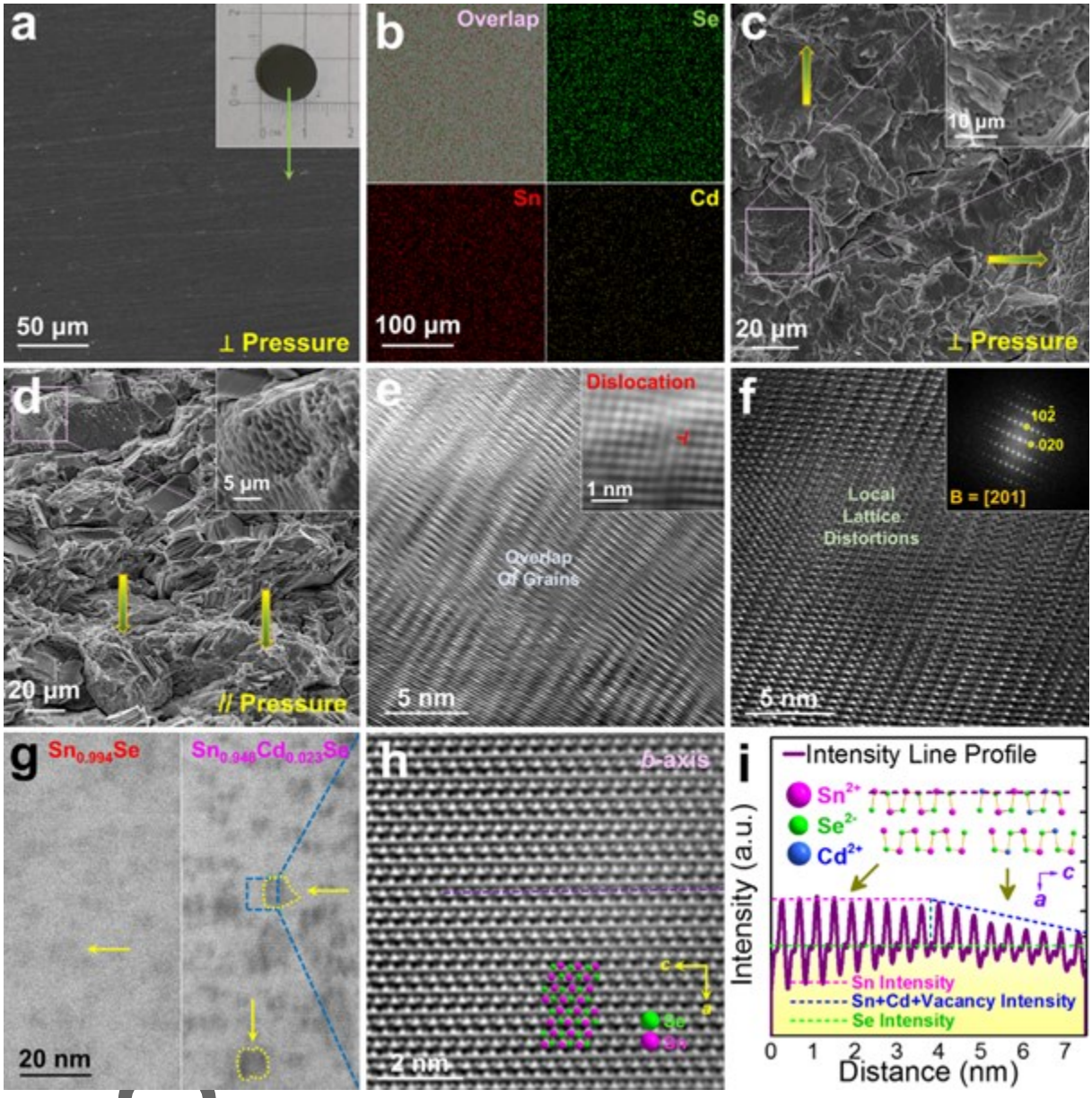

Figure 7. Morphological and compositional characterizations of sintered pellets. (a) SEM image with inset of optical image of $Sn_{0.948}Cd_{0.023}Se$ pellet polished from the ⊥ direction; (b) Corresponding EDS mapping results for (a); SEM images of $Sn_{0.948}Cd_{0.023}Se$ pellet fractured from (c) the ⊥ direction and (d) the // direction, the inset magnified SEM images show the honeycomb-like structure; (e) TEM image of sliced $Sn_{0.948}Cd_{0.023}Se$ pellet to see the overlap of grains with inset HRTEM image showing a typical dislocation; (f) HRTEM image to show the local lattice distortion; (g) Comparison of Cs-

STEM HAADF images between $Sn_{0.994}Se$ (left) and $Sn_{0.948}Cd_{0.023}Se$ (right) pellets to see the difference; (h) High resolution Cs-STEM HAADF image of $Sn_{0.948}Cd_{0.023}Se$ pellet viewed along the *b*-axis to see different contrast; and (i) corresponding intensity line profile taken from (h) to illustrate the potential reasons causing the contrast difference.

We measured σ, S, $S^2\sigma$, and κ as the main thermoelectric properties from 300 K to 873 K for the Cd-doped SnSe pellets with different doping levels and the results are shown in **Figure 8(a-d)**, respectively. High repeatability was realized with measured fluctuations being 10 %, 2 % and 5 % for σ, S and κ, respectively, as shown in **Figure S6**. Besides, considering the anisotropy shown in **Figure S7**,[7, 14] the ⊥ direction is chosen as the main direction for measurements.[51] **Figure 8(a)** shows *T*-dependent σ. After Cd doping, σ was significantly improved due to the improved cation vacancy concentration. As can be seen, the totality of σ values includes two regions. Taking $Sn_{0.948}Cd_{0.023}Se$ as an example, a representative metallic transport behavior can be seen before 723 K, derived from the vibration of cations, which can effectively impede the transport of carriers.[14] After 723 K, a classic thermally-activated semiconducting behavior is observed, derived from the carrier thermal excitation by heat, which can produce extra carriers and improve the carrier concentration. The temperature between these two regions (723 K in the case of $Sn_{0.948}Cd_{0.023}Se$) is described as bipolar-effect temperature (T*), where T* increases from 623 K to 723 K with increasing the doping level (cation vacancy concentration), fitting well with reported calculation-based works.[3] **Figure 8(b)** shows the measured *T*-dependent S, in which peak S values can be achieved at T*. With increasing the Cd doping level, S gradually decreased, accompanied by a slight shifting of T* towards a higher T, indicating an increase of p.[3, 7] **Figure 8(c)** shows the determined $S^2\sigma$, from which two peak values of 7.33 μW cm^{-1} K^{-2} at 423 K and 6.86 μW cm^{-1} K^{-2} at 823 K can be found in the $Sn_{0.948}Cd_{0.023}Se$ pellet. **Figure 8(d)** shows the calculated *T*-dependent κ *via* $\kappa = D \cdot C_p \cdot \rho$ [7], where measured D values are plotted in **Figure S8(a)**,

and measured C_p and ρ are listed in **Table 2**. As can be seen, with an increasing Cd doping level, κ decreases, derived from the enhanced nanoscale crystal imperfections including locally distorted lattice, dislocations, and point defects. These nanoscale defects can effectively strengthen the scattering of phonons from medium and short wavelengths. Considering the high relative densities in our sintered pellets (all > 97.1 %),[14, 19] the κ values are intrinsic.

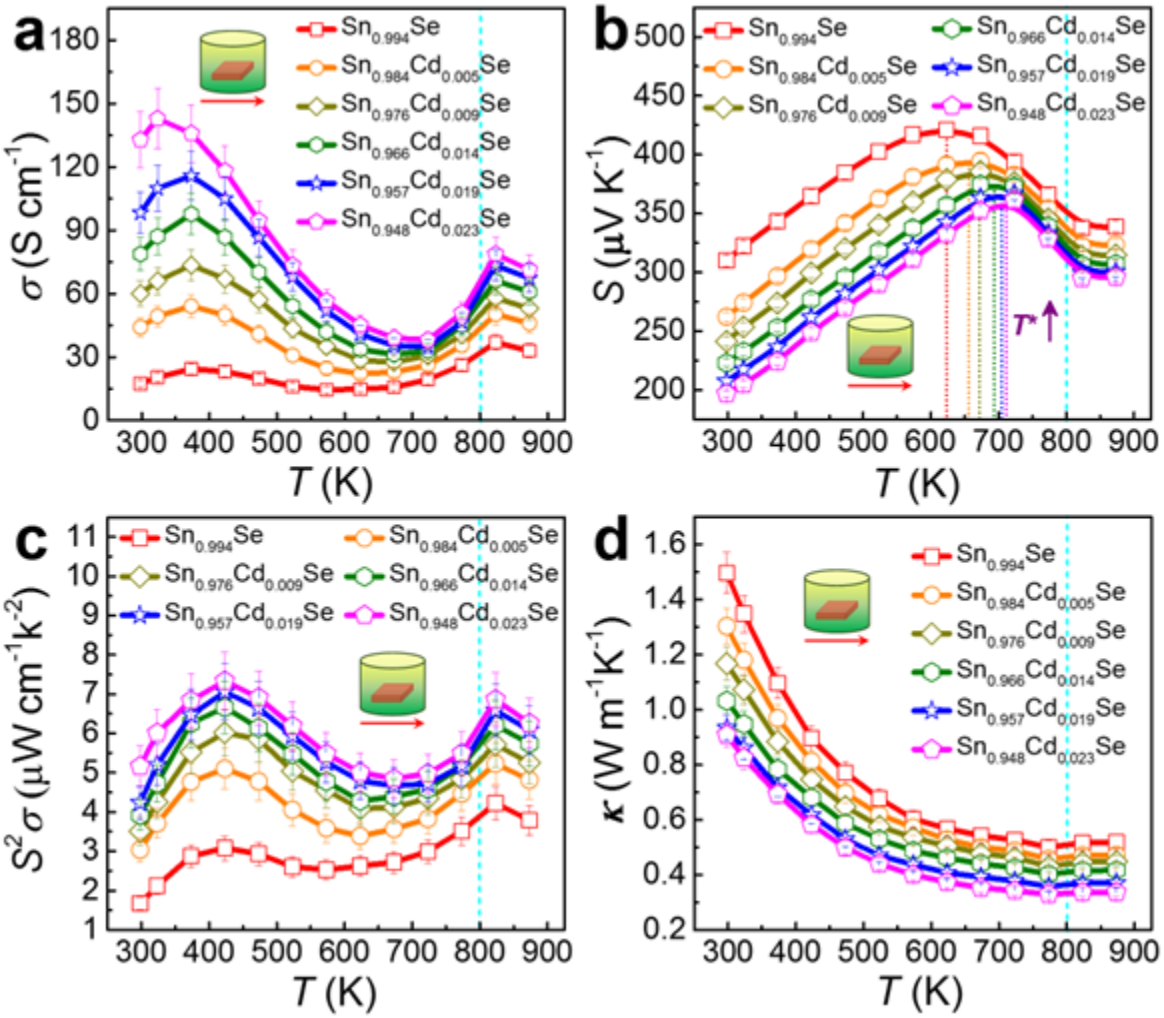

Figure 8. Plots of measured *T*-dependent properties from Cd-doped SnSe pellets: (a) σ; (b) S; (c) $S^2\sigma$; and (d) κ.

Table 2. The main properties of Cd-doped SnSe at both 300 K and 823 K.

Parameters	$Sn_{0.994}Se$	$Sn_{0.984}Cd_{0.005}Se$	$Sn_{0.976}Cd_{0.009}Se$	$Sn_{0.966}Cd_{0.014}Se$	$Sn_{0.957}Cd_{0.019}Se$	$Sn_{0.948}Cd_{0.023}Se$
ρ (g cm^{-3})	6.121	6.103	6.077	6.045	6.021	6.002
$p_{300\ K}$ (cm^{-3})	2.79×10^{18}	7.29×10^{18}	9.98×10^{18}	1.33×10^{19}	1.71×10^{19}	2.33×10^{19}
$p_{823\ K}$ (cm^{-3})	7.71×10^{18}	1.17×10^{19}	1.48×10^{19}	1.91×10^{19}	2.25×10^{19}	2.60×10^{19}
$\mu_{300\ K}$ (cm^2 V^{-1} s^{-1})	39.0	37.8	37.6	37.0	35.9	35.5
$\mu_{823\ K}$ (cm^2 V^{-1} s^{-1})	29.9	26.8	24.4	21.7	20.4	18.9
$\sigma_{300\ K}$ (S cm^{-1})	17.4	44.2	60.1	78.8	98.3	132.9
$\sigma_{823\ K}$ (S cm^{-1})	37.0	50.3	58.0	62.2	73.4	78.8
$S_{300\ K}$ (μV K^{-1})	310.0	262.2	241.6	223.0	207.5	197.1
$S_{823\ K}$ (μV K^{-1})	337.9	322.5	313.8	306.2	299.5	295.1
$S^2\sigma_{300\ K}$ (μW cm^{-1} K^{-2})	1.67	3.04	3.51	3.92	4.23	5.16
$S^2\sigma_{823\ K}$ (μW cm^{-1} K^{-2})	4.22	5.23	5.71	6.20	6.58	6.86
$C_{p300\ K}$ (J g^{-1} K^{-1})	0.273	0.27	0.267	0.263	0.259	0.254
$C_{p823\ K}$ (J g^{-1} K^{-1})	0.286	0.281	0.277	0.272	0.268	0.264
$\kappa_{300\ K}$ (W m^{-1} K^{-1})	1.50	1.30	1.17	1.03	0.93	0.91
$\kappa_{823\ K}$ (W m^{-1} K^{-1})	0.52	0.47	0.45	0.42	0.37	0.33

To better understand our achieved electrical transport properties, we measured the *T*-dependent *p*. The result is shown in **Figure 9(a)**. A slightly increased *p* after *T** can be seen, triggered by thermal activation.[3] With increasing the Cd doping level, *p* is improved, caused by the higher cation vacancy con-

centration. **Figure 9(b)** shows the corresponding T-dependent carrier mobility μ, which roughly follows the power law ($\mu \propto T^{d}$).[25, 52] At low temperatures, μ is slightly increased, roughly following $\mu \propto T^{1.1}$, suggesting that the ionized impurities dominate the scattering mechanism.[25, 52] At medium temperatures, μ is decreased following $\mu \propto T^{-1.5}$, meaning that acoustic-phonon scattering dominates the scattering mechanism instead.[25, 52] At high temperatures, μ increases roughly following $\mu \propto T^{1.5}$, indicating extra scattering behaviors. Potential carrier scattering at local crystal imperfections observed in the Cd-doped SnSe may cause a special $\mu \propto T^{d}$ relation.[25, 53, 54] Besides, μ decreases with increasing Cd doping level, which is caused by the significant blocking and/or scattering of carriers. At high temperature, because the thermal activation can provide additional carriers (mainly holes as majority carriers),[3] with increasing doping level (cation vacancy concentration), additional carriers can be released, resulting in a lower μ between 600 and 800 K.

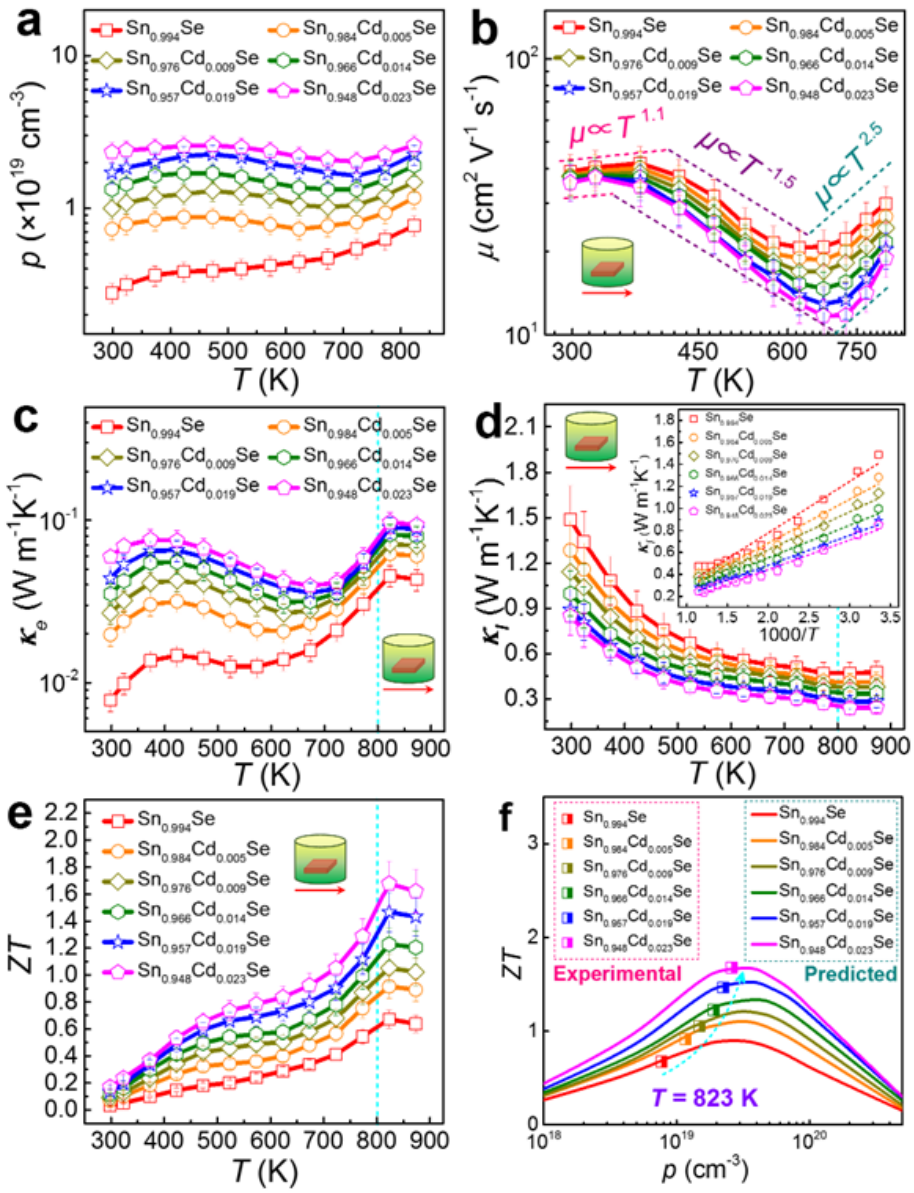

Figure 9. Plots of measured and/or calculated *T*-dependent properties for Cd-doped SnSe pellets: (a) p; (b) μ; (c) κ_e; (d) κ_l with 1000/T-dependent κ_l as inset; and (e) ZT. (f) A comparison of achieved ZTs with calculated predicted ZTs.

To further understand the electronic structure and DOS evolution of the Cd-doped SnSe with different cation vacancy concentrations, we performed DFT calculations. **Figure 10(a-c)** compares the calculated band structures for $Sn_{0.994}Se$, $Sn_{0.976}Cd_{0.009}Se$, and $Sn_{0.957}Cd_{0.019}Se$, respectively, and **Figure 10(d)** compares the DOS of $Sn_{0.994}Se$, $Sn_{0.984}Cd_{0.005}Se$, $Sn_{0.976}Cd_{0.009}Se$, $Sn_{0.966}Cd_{0.014}Se$, $Sn_{0.957}Cd_{0.019}Se$, and $Sn_{0.948}Cd_{0.023}Se$, respectively. It is clear that the Fermi level moves towards the valence band with increaing cation vacancy concentration, indicating a degenerate semiconductor which can provide more holes, contributing to an improved p and in turn an enhanced $S^2\sigma$, agreeing with the experimental results shown in **Figure 9**.

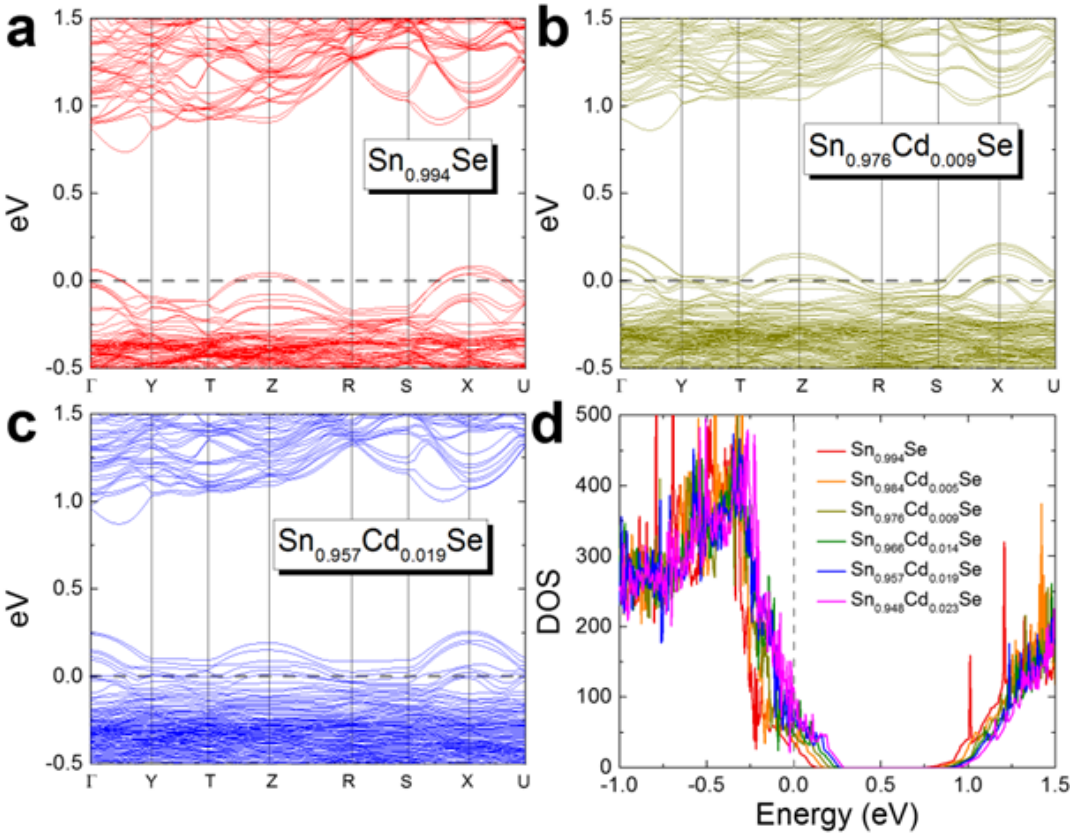

Figure 10. Comparisons of calculated band structures for (a) $Sn_{0.994}Se$, (b) $Sn_{0.976}Cd_{0.009}Se$ and (c) $Sn_{0.957}Cd_{0.019}Se$; and (d) comparisons of DOS of $Sn_{0.994}Se$, $Sn_{0.984}Cd_{0.005}Se$, $Sn_{0.976}Cd_{0.009}Se$, $Sn_{0.966}Cd_{0.014}Se$, $Sn_{0.957}Cd_{0.019}Se$, and $Sn_{0.948}Cd_{0.023}Se$.

For the thermal transport performance, κ_e and κ_l are investigated to further understand the contributions of electrons and lattice on the total thermal conductivity κ. κ_e is obtained *via* $\kappa_e = L \cdot \sigma \cdot T$ by the Wiedemann-Franz law.[3] Here L is the Lorenz number (~1.5×10^{-8} V^2 K^{-2}) calculated *via* the SPB model[42-44] as shown in **Figure S8(c)**, and κ_l is determined by $\kappa_l = \kappa - \kappa_e$. **Figure 9(c)** shows the determined κ_e with very low values, which have the same trend compared with the corresponding σ. **Figure 9(d)** shows the determined T-dependent κ_l, with the inset showing the determined 1000/T-dependent κ_l roughly following a linear relationship, showing that Umklapp phonon scattering dominates phonon scattering in SnSe.[26, 55] Such intrinsic low κ_l have been derived from significantly anharmonic bonding[3, 7, 14, 21, 23, 26] and the observed nanoscale crystal imperfections including the dislocations, local lattice distortions, point defects (vacancy domains), grain boundaries and/or interfaces, which can effectively scatter phonons of different wavelengths.[1, 3] The calculated κ_l /κ ratio of > ~70 % (refer to **Figure S8(d)**), indicates that phonon transport is significant for κ.

Figure 9(e) presents the calculated T-dependent ZT values for the Cd-doped SnSe pellets, indicating that the improved cation vacancy concentration is critical for securing a high ZT value. The high ZTs (>0.6) are in a wide range from 450 K to 873 K, which is of significance because the device has to be operated under a large temperature gradient.[1, 3] **Figure 9(f)** compares the achieved ZT values with predicted values determined by the SPB model-based calculations at 823 K.[42-45] As can be seen, the measured p = ~2.6×10^{19} cm^{-3} is much closer to the best value of ~3×10^{19} cm^{-3} as we calculated, indicating that p can be indeed tuned through our developed methodology. **Table 3** compares our achieved thermoelectric properties with reported studies, showing a strong competitiveness in our polycrystalline Cd-doped SnSe fabricated *via* a facile solvothermal synthesis. It should be mentioned that SnSe is a typical low-toxic and high cost-effective thermoelectric material.[3, 51] Even though Cd is

a toxic element,[56] the amount of Cd in our SnSe system is very low (only ~2.3 %), thus our Cd-doped SnSe is still a green thermoelectric material.

Table 3. A comparison of performance from *p*-type doped polycrystalline SnSe. Here ST, HT, M, ZM, A, SSR, MA, HP mean solvothermal, hydrothermal, melting, zone-melting, annealing, solid-state solution, mechanical alloying, and hot-pressing, respectively. The * means the room temperature-measured *p*.

Product	Synthetic Method	*ZT*	*T* (K)	σ (S cm^{-1})	*S* (μV K^{-1})	$S^2\sigma$ (mW m^{-1} K^{-2})	κ (W m^{-1} K^{-1})	*p* (10^{19} cm^{-3})	ρ (g cm^{-3})	Ref.
$Sn_{0.948}Cd_{0.023}Se$	ST+SPS	1.7	823	~78.8	~295.1	~0.69	~0.33	~2.60	~6.00	This work
$Sn_{0.99}Na_{0.01}Se$	M+SPS	0.75	823	~49.6	~311.1	0.48	~0.53	1.0*	~5.99	[57]
$Sn_{0.99}Na_{0.01}Se$	M+SPS	~0.8	800	~81.2	~267.2	~0.58	~0.50	~1.5	-	[12]
$Sn_{0.99}Na_{0.01}Se$	M+A+SPS	0.85	800	~100.4	~271.5	~0.74	~0.50	~6.5*	5.94	[58]
$Sn_{0.985}Na_{0.015}Se$	M+MA+HP	~0.8	773	~37.9	~298.8	~0.34	~0.33	~2.1*	5.81	[59]
$Sn_{0.98}Na_{0.02}Se$	SPS	0.87	798	~56.4	~288.8	0.47	0.4	3.08*	~5.81	[60]
$Sn_{0.97}Na_{0.03}Se$	SPS	0.82	773	~65.1	~280.2	~0.51	~0.50	~2.2	~5.93	[61]
$Sn_{0.99}Na_{0.005}K_{0.005}Se$	MA+SPS	1.2	773	~34.9	~374.7	~0.49	0.32	~7.2*	5.71	[37]
$Sn_{0.995}Na_{0.005}SeCl_{0.005}$	SSR+HP	0.84	810	~79.2	~228.6	~0.41	~0.39	~3.95*	~5.93	[62]
$Sn_{0.99}Na_{0.01}Se_{0.84}Te_{0.16}$	MA+SPS	0.72	773	~67.4	~275.0	~0.51	~0.50	-	-	[13]
$(Sn_{0.96}Pb_{0.04})_{0.99}Na_{0.01}Se$	M+SPS	~1.2	773	~89.4	~269.7	~0.65	~0.45	~2.8	-	[63]
$Sn_{0.99}K_{0.01}Se$	MA+SPS	~1.1	773	~18.6	~421.4	~0.33	~0.24	0.92*	-	[64]
$SnSe_{0.985}Cl_{0.015}$	M	1.1	773	~25.5	~399.3	~0.41	~0.30	~0.01*	5.87	[36]

$Sn_{0.99}Zn_{0.01}Se$	M+HP	0.96	873	~74.1	~328.5	0.8	~0.73	~0.45	-	[40]
$Sn_{0.9}Ge_{0.1}Se$	M	-	400	-	~843.2	-	~0.39	-	-	[65]
$Sn_{0.96}Ge_{0.04}Se$	ZM+HP	0.6	823	35.6	~378.5	0.51	~0.7	~0.03*	>5.81	[39]
$Sn_{0.99}Cu_{0.01}Se$	HT+HP	1.2	873	~36.4	~313.8	~0.35	~0.2	-	-	[66]
$Sn_{0.98}Cu_{0.02}Se$	M+A+SPS	0.7	773	~42.4	~238.6	~0.24	0.27	18.4*	~6.12	[67]
$Sn_{0.97}Cu_{0.03}Se$	M+HP	0.79	823	~35.0	~325.1	~0.37	~0.39	~0.016*	6.16	[68]
$Sn_{0.99}Ag_{0.01}Se$	M+A+HP	0.6	750	~45.9	~344.1	~0.54	~0.68	~0.35*	~5.93	[69]
$Sn_{0.99}Ag_{0.01}Se$	M+A+SPS	0.74	823	~54.8	~330.9	0.6	~0.66	1.9*	~5.99	[70]
$Sn_{0.985}Ag_{0.015}Se$	M	1.3	773	~44.7	~344.0	~0.52	~0.30	~0.8*	5.87	[36]
$Sn_{0.97}Ag_{0.03}Se$	ST+SPS	0.8	850	~90.3	~266.2	~0.64	~0.68	0.9*	>5.56	[71]
$Sn_{0.995}Tl_{0.005}Se$	M+HP	0.6	725	~68.9	~300.0	~0.62	~0.75	-	~5.99	[72]
$Sn_{0.99}In_{0.01}Se$	M+HP	0.2	823	~6.53	~350.0	~0.08	~0.36	~0.03*	~5.87	[73]
$Sn_{0.97}Sm_{0.03}Se$	M+HP	0.55	823	~33.6	~250.0	~0.21	~0.32	~0.013*	-	[47]
$SnSe_{0.9}Te_{0.1}$	ST+SPS	1.1	800	~57.4	~322.8	~0.60	~0.44	~1*	~5.87	[38]

3. Conclusion

In this study, a combination of cation vacancy engineering and local lattice engineering is used to realize excellent thermoelectric properties in *p*-type polycrystalline Cd-doped SnSe *via* a facile solvothermal synthesis method and a fast spark plasma sintering technique. The Cd solubility in SnSe is ~2.3 at. % with a high cation vacancy concentration of ~2.9 %, contributing to a high hole carrier concentration of ~2.6×10^{19} cm^{-3} and in turn leading a high power factor of ~6.9 μW cm^{-1} K^{-2} at 823 K. Meanwhile, the doped Cd results in massive nanoscale crystal imperfections including dislocations, intensive local lattice distortions, and point defects, which contribute to a low thermal conductivity of

~0.33 W m^{-1} K^{-1} and in turn a record high *ZT* of ~1.7 at this temperature. This study explores the fundamental Cd-doping mechanisms at a nanoscale in a SnSe matrix and describes a novel concept to achieve high *ZT*.

4. Experimental Section

The experimental details can be seen in **Section 9** in Supporting Information.

Supporting Information.

Supporting Information is available from the Wiley Online Library or from the author.

Notes

The authors declare no competing financial interest.

Acknowledgements

X. L. S. and A. Y. W. contributed equally to this work. This work was financially supported by the Australian Research Council and the National Natural Science Foundation of China (11774016). XLS thanks the IPRS for providing his PhD program. The Australian Microscopy & Microanalysis Research Facility is acknowledged for providing characterization facilities. Theoretical work by T. L. F. and S. T. P. is supported in part by Department of Energy grant DE-FG0209ER46554 and by the McMinn Endowment. Computations at Vanderbilt University and ORNL were performed at the National Energy Research Scientific Computing Center (NERSC), a Department of Energy, Office of Science, User Facility funded through Contract No. DE-AC02-05CH11231. Computations also used the Extreme Science and Engineering Discovery Environment (XSEDE).

Received: ((will be filled in by the editorial staff))
Revised: ((will be filled in by the editorial staff))
Published online: ((will be filled in by the editorial staff))

Reference

[1] T. Zhu, Y. Liu, C. Fu, J.P. Heremans, J.G. Snyder, X. Zhao, *Adv. Mater.* **2017**, *29,* 1605884.

[2] L.-D. Zhao, V.P. Dravid, M.G. Kanatzidis, *Energy Environ. Sci.* **2014**, *7,* 251-268.

[3] Z.-G. Chen, X. Shi, L.-D. Zhao, J. Zou, *Prog. Mater. Sci.* **2018**, *97,* 283-346.

[4] R. Moshwan, L. Yang, J. Zou, Z.-G. Chen, *Adv. Funct. Mater.* **2017**, *27,* 1703278.

[5] K. Zhao, H. Duan, N. Raghavendra, P. Qiu, Y. Zeng, W. Zhang, J. Yang, X. Shi, L. Chen, *Adv. Mater.* **2017**, *29,* 1701148.

[6] M.S. Dresselhaus, G. Chen, M.Y. Tang, R.G. Yang, H. Lee, D.Z. Wang, Z.F. Ren, J.P. Fleurial, P. Gogna, *Adv. Mater.* **2007**, *19,* 1043-1053.

[7] X. Shi, Z. Chen, W. Liu, L. Yang, M. Hong, R. Moshwan, L. Huang, J. Zou, *Energy Storage Mater.* **2018**, *10,* 130-138.

[8] W.D. Liu, Z.G. Chen, J. Zou, *Adv. Energy Mater.* **2018**, 1800056.

[9] K. Kutorasinski, B. Wiendlocha, S. Kaprzyk, J. Tobola, *Phys. Rev. B* **2015**, *91,* 205201.

[10] Y. Zhou, L.-D. Zhao, *Adv. Mater.* **2017**, *29,* 1702676.

[11] T.-R. Wei, C.-F. Wu, F. Li, J.-F. Li, *J. Materiomics* **2018**, *4,* 304-320.

[12] T.R. Wei, G. Tan, X. Zhang, C.F. Wu, J.F. Li, V.P. Dravid, G.J. Snyder, M.G. Kanatzidis, *J. Am. Chem. Soc.* **2016**, *138,* 8875-8882.

[13] T.R. Wei, C.F. Wu, X. Zhang, Q. Tan, L. Sun, Y. Pan, J.F. Li, *Phys. Chem. Chem. Phys.* **2015**, *17,* 30102-30109.

[14] L.D. Zhao, S.H. Lo, Y. Zhang, H. Sun, G. Tan, C. Uher, C. Wolverton, V.P. Dravid, M.G. Kanatzidis, *Nature* **2014**, *508,* 373-377.

[15] C. Chang, M. Wu, D. He, Y. Pei, C.-F. Wu, X. Wu, H. Yu, F. Zhu, K. Wang, Y. Chen, *Science* **2018**, *360,* 778-783.

[16] L.-D. Zhao, C. Chang, G. Tan, M.G. Kanatzidis, *Energy Environ. Sci.* **2016**, *9,* 3044-3060.

[17] S. Sassi, C. Candolfi, J.B. Vaney, V. Ohorodniichuk, P. Masschelein, A. Dauscher, B. Lenoir, *Appl. Phys. Lett.* **2014**, *104,* 212105.

[18] L.-D. Zhao, G. Tan, S. Hao, J. He, Y. Pei, H. Chi, H. Wang, S. Gong, H. Xu, V.P. Dravid, *Science* **2016**, *351,* 141-144.

[19] P.-C. Wei, S. Bhattacharya, J. He, S. Neeleshwar, R. Podila, Y. Chen, A. Rao, *Nature* **2016**, *539,* E1-E2.

[20] D. Ibrahim, J.-B. Vaney, S. Sassi, C. Candolfi, V. Ohorodniichuk, P. Levinsky, C. Semprimoschnig, A. Dauscher, B. Lenoir, *Appl. Phys. Lett.* **2017**, *110,* 032103.

[21] X.L. Shi, K. Zheng, W.D. Liu, Y. Wang, Y.Z. Yang, Z.G. Chen, J. Zou, *Adv. Energy Mater.* **2018**, *8,* 1800775.

[22] C. Chang, Q. Tan, Y. Pei, Y. Xiao, X. Zhang, Y.-X. Chen, L. Zheng, S. Gong, J.-F. Li, J. He, *RSC Adv.* **2016**, *6,* 98216-98220.

[23] X.L. Shi, K. Zheng, M. Hong, W.D. Liu, R. Moshwan, Y. Wang, X.-L. Qu, Z.G. Chen, J. Zou, *Chem. Sci.* **2018**, *9,* 7376-7389.

[24] Y.-M. Han, J. Zhao, M. Zhou, X.-X. Jiang, H.-Q. Leng, L.-F. Li, *J. Mater. Chem. A* **2015**, *3,* 4555-4559.

[25] Y. Li, F. Li, J. Dong, Z. Ge, F. Kang, J. He, H. Du, B. Li, J.-F. Li, *J. Mater. Chem. C* **2016**, *4,* 2047-2055.

[26] K. Peng, X. Lu, H. Zhan, S. Hui, X. Tang, G. Wang, J. Dai, C. Uher, G. Wang, X. Zhou, *Energy Environ. Sci.* **2016**, *9,* 454-460.

[27] A.T. Duong, V.Q. Nguyen, G. Duvjir, V.T. Duong, S. Kwon, J.Y. Song, J.K. Lee, J.E. Lee, S. Park, T. Min, J. Lee, J. Kim, *Nat. Commun.* **2016**, *7,* 13713.

[28] L. Yang, Z.-G. Chen, M.S. Dargusch, J. Zou, *Adv. Energy Mater.* **2017**, *8,* 1701797.

[29] B. Li, Y. Xie, J. Huang, Y. Qian, *Inorg. Chem.* **2000**, *39,* 2061-2064.

[30] J. Dai, J. Sun, A. Xie, J. He, C. Li, Y. Yan, *RSC Adv.* **2016**, *6,* 3446-3457.

[31] T. Schröder, T. Rosenthal, N. Giesbrecht, M. Nentwig, S. Maier, H. Wang, G.J. Snyder, O. Oeckler, *Inorg. Chem.* **2014**, *53,* 7722-7729.

[32] W. Wei, C. Chang, T. Yang, J. Liu, H. Tang, J. Zhang, Y. Li, F. Xu, Z. Zhang, J.-F. Li, *J. Am. Chem. Soc.* **2017**, *140,* 499-505.

[33] N.V. Quang, D.A. Tuan, D.V. Thiet, N.T. Minh Hai, G. Duvjir, T.T. Ly, K. Jungdae, C. Sunglae, *Bull. Am. Phys. Soc.* **2017**, *62*.

[34] Q. Li, L. Zhang, J. Yin, Z. Sheng, X. Chu, F. Wang, F. Zhu, *J. Alloy. Compd.* **2018**, *745,* 513-518.

[35] A. TakeuchiA. Inoue, *Mater. Trans.* **2005**, *46,* 2817-2829.

[36] L. Zhang, J. Wang, Q. Sun, P. Qin, Z. Cheng, Z. Ge, Z. Li, S. Dou, *Adv. Energy Mater.* **2017**, *7,* 1700573.

[37] Z.-H. Ge, D. Song, X. Chong, F. Zheng, L. Jin, X. Qian, L. Zheng, R.E. Dunin-Borkowski, P. Qin, J. Feng, *J. Am. Chem. Soc.* **2017**, *139,* 9714-9720.

[38] M. Hong, Z.-G. Chen, L. Yang, T.C. Chasapis, S.D. Kang, Y. Zou, G.J. Auchterlonie, M.G. Kanatzidis, G.J. Snyder, J. Zou, *J. Mater. Chem. A* **2017**, *5,* 10713-10721.

[39] Y. Fu, J. Xu, G.-Q. Liu, X. Tan, Z. Liu, X. Wang, H. Shao, H. Jiang, B. Liang, J. Jiang, *J. Electron. Mater.* **2017**, *46,* 3182-3186.

[40] J.C. Li, D. Li, X.Y. Qin, J. Zhang, *Scripta Mater.* **2017**, *126,* 6-10.

[41] G. Tang, W. Wei, J. Zhang, Y. Li, X. Wang, G. Xu, C. Chang, Z. Wang, Y. Du, L.-D. Zhao, *J. Am. Chem. Soc.* **2016**, *138,* 13647-13654.

[42] Y. Xu, W. Li, C. Wang, J. Li, Z. Chen, S. Lin, Y. Chen, Y. Pei, *J. Mater. Chem. A* **2017**, *5,* 19143-19150.

[43] J. Shen, Z. Chen, S. lin, L. Zheng, W. Li, Y. Pei, *J. Mater. Chem. C* **2016**, *4,* 209-214.

[44] X. She, X. Su, H. Du, T. Liang, G. Zheng, Y. Yan, R. Akram, C. Uher, X. Tang, *J. Mater. Chem. C* **2015**, *3,* 12116-12122.

[45] L. Zhao, S.M.K.N. Islam, J. Wang, D.L. Cortie, X. Wang, Z. Cheng, J. Wang, N. Ye, S. Dou, X. Shi, L. Chen, G.J. Snyder, X. Wang, *Nano Energy* **2017**, *41,* 164-171.

[46] D.G. Cahill, S.K. Watson, R.O. Pohl, *Phys. Rev. B* **1992**, *46,* 6131.

[47] J. Gao, H. Zhu, T. Mao, L. Zhang, J. Di, G. Xu, *Mater. Res. Bull.* **2017**, *93,* 366-372.

[48] J. Yang, L. Fei, H. Liu, Y. Liu, M. Gao, Y. Zhang, L. Yang, *J. Alloy. Compd.* **2011**, *509,* 3672-3676.

[49] S. HillyardJ. Silcox, *Ultramicroscopy* **1995**, *58,* 6-17.

[50] P. NellistS. Pennycook, *Ultramicroscopy* **1999**, *78,* 111-124.

[51] X. Shi, A. Wu, W. Liu, R. Moshwan, Y. Wang, Z.-G. Chen, J. Zou, *ACS Nano* **2018**, *12,* 11417-11425.

[52] M. Nassary, *Turk. J. Phys.* **2009**, *33,* 201-208.

[53] Q. Tan, L.-D. Zhao, J.-F. Li, C.-F. Wu, T.-R. Wei, Z.-B. Xing, M.G. Kanatzidis, *J. Mater. Chem. A* **2014**, *2,* 17302-17306.

[54] J. Martin, L. Wang, L. Chen, G. Nolas, *Phys. Rev. B* **2009**, *79,* 115311.

[55] D.R. Clarke, *Surf. Coat. Tech.* **2003**, *163,* 67-74.

[56] P. Das, S. Samantaray, G. Rout, *Environ. Pollut.* **1997**, *98,* 29-36.

[57] H.-Q. Leng, M. Zhou, J. Zhao, Y.-M. Han, L.-F. Li, *RSC Adv.* **2016**, *6,* 9112-9116.

[58] T.-R. Wei, G. Tan, C.-F. Wu, C. Chang, L.-D. Zhao, J.-F. Li, G.J. Snyder, M.G. Kanatzidis, *Appl. Phys. Lett.* **2017**, *110,* 053901.

[59] E.K. Chere, Q. Zhang, K. Dahal, F. Cao, J. Mao, Z. Ren, *J. Mater. Chem. A* **2016**, *4,* 1848-1854.

[60] B. Cai, J. Li, H. Sun, P. Zhao, F. Yu, L. Zhang, D. Yu, Y. Tian, B. Xu, *J. Alloy. Compd.* **2017**, *727,* 1014-1019.

[61] K. Peng, H. Wu, Y. Yan, L. Guo, G. Wang, X. Lu, X. Zhou, *J. Mater. Chem. A* **2017**, *5,* 14053-14060.

[62] S.D. Yang, R.K. Nutor, Z.J. Chen, H. Zheng, H.F. Wu, J.X. Si, *J. Electron. Mater.* **2017**, *46,* 6662-6668.

[63] Y.K. Lee, K. Ahn, J. Cha, C. Zhou, H.S. Kim, G. Choi, S.I. Chae, J.-H. Park, S.-P. Cho, S.H. Park, Y.-E. Sung, W.B. Lee, T. Hyeon, I. Chung, *J. Am. Chem. Soc.* **2017**, *139,* 10887-10896.

[64] Y.-X. Chen, Z.-H. Ge, M. Yin, D. Feng, X.-Q. Huang, W. Zhao, J. He, *Adv. Funct. Mater.* **2016**, *26,* 6836-6845.

[65] M. Gharsallah, F. Serrano-Sanchez, N.M. Nemes, F.J. Mompean, J.L. Martinez, M.T. Fernandez-Diaz, F. Elhalouani, J.A. Alonso, *Sci. Rep.* **2016**, *6,* 26774.

[66] Y. Gong, C. Chang, W. Wei, J. Liu, W. Xiong, S. Chai, D. Li, J. Zhang, G. Tang, *Scripta Mater.* **2018**, *147,* 74-78.

[67] N.K. Singh, S. Bathula, B. Gahtori, K. Tyagi, D. Haranath, A. Dhar, *J. Alloy. Compd.* **2016**, *668,* 152-158.

[68] J. GaoG. Xu, *Intermetallics.* **2017**, *89,* 40-45.

[69] C.-L. Chen, H. Wang, Y.-Y. Chen, T. Day, G.J. Snyder, *J. Mater. Chem. A* **2014**, *2,* 11171.

[70] H. Leng, M. Zhou, J. Zhao, Y. Han, L. Li, *J. Electron. Mater.* **2015**, *45,* 527-534.

[71] C.-H. Chien, C.-C. Chang, C.-L. Chen, C.-M. Tseng, Y.-R. Wu, M.-K. Wu, C.-H. Lee, Y.-Y. Chen, *RSC Adv.* **2017**, *7,* 34300-34306.

[72] V. Kucek, T. Plechacek, P. Janicek, P. Ruleova, L. Benes, J. Navratil, C. Drasar, *J. Electron. Mater.* **2016**, *45,* 2943-2949.

[73] J.H. Kim, S. Oh, Y.M. Kim, H.S. So, H. Lee, J.-S. Rhyee, S.-D. Park, S.-J. Kim, *J. Alloy. Compd.* **2016**, *682,* 785-790.

The table of contents

We achieve high Figure of Merit (*ZT*) of ~1.7 at 823 K in *p*-type Cd-doped SnSe microplates via tuning high carrier concentration of ~2.6×10^{19} cm^{-3} by improving cation vacancy rate and realizing low thermal conductivity of ~0.33 W m^{-1} K^{-1} by inducing intensive local crystal defects including lattice distortions, dislocations, and point defects.

Thermoelectrics

X. Shi, A. Wu, T. Feng, K. Zheng, W. Liu, Q. Sun, M. Hong, S. T. Pantelides, Z.-G. Chen*, J. Zou*

High thermoelectric performance in *p*-type polycrystalline Cd-doped SnSe achieved by a combination of cation vacancies and localized lattice engineering